Applied Catalysis B: Environmental 300 (2022) 120734

Contents lists available at ScienceDirect

Applied Catalysis B: Environmental

journal homepage: www.elsevier.com/locate/apcatb

Highly efficient adsorption and catalytic degradation of ciprofloxacin by a novel heterogeneous Fenton catalyst of hexapod-like pyrite nanosheets mineral clusters

Xin Nie [a], Guiying Li [b], Shanshan Li [c], Yingmei Luo [c], Wenming Luo [c], Quan Wan [a,d,*], Taicheng An [b,**]

[a] State Key Laboratory of Ore Deposit Geochemistry, Institute of Geochemistry, Chinese Academy of Sciences, Guiyang 550081, China
[b] Guangdong Key Laboratory of Environmental Catalysis and Health Risk Control, Guangzhou Key Laboratory Environmental Catalysis and Pollution Control, School of Environmental Science and Engineering, Institute of Environmental Health and Pollution Control, Guangdong University of Technology, Guangzhou 510006, China
[c] School of Chemistry and Materials Science, Guizhou Normal University, Guiyang 550001, China
[d] CAS Center for Excellence in Comparative Planetology, Hefei 230026, China

ARTICLE INFO

Keywords:
Pyrite mineral
Hexapod-like nanosheets clusters
Heterogeneous Fenton catalyst
Ciprofloxacin degradation kinetics
Degradation mechanism

ABSTRACT

Herein, a novel hexapod-like pyrite nanosheets mineral cluster was prepared *via* a facile hydrothermal method. Compared with classical homogeneous Fenton processes, this catalyst possessed a higher adsorption capacity and catalytic activity to ciprofloxacin (20 mg/L), which could be completely degraded within 10 min at pH 4.0. $^{\bullet}OH$ was the main reactive oxygen species responsible for ciprofloxacin degradation. Br^- ($\geq$ 1 mM), I^- ($\geq$ 1 mM), and high concentration of F^- ions ($\geq$ 10 mM) exhibited an inhibition effect on ciprofloxacin degradation, but the Cl^- ions (0–100 mM) did not show obvious effects on ciprofloxacin removal. Thirteen intermediates were qualitatively identified, and degradation mechanism was tentatively proposed for ciprofloxacin. Several toxic intermediates were produced, but they could be fully mineralized and detoxified by this heterogeneous Fenton catalyst after 30 min reaction. The work provides a novel heterogeneous Fenton catalyst to purify and detoxify antibiotics as well as other refractory organic pollutants contaminated wastewater.

1. Introduction

Antibiotics, as a kind of widely used pharmaceutical drugs and refractory organic pollutants (ROPs) presented in various aquatic environments, have received much attention about their environmental fate and toxicological properties [1,2]. Antibiotics could be entered into the recipient environments through excretion and/or improper disposal of outdated or unused medication, municipal and industrial wastewater, excreta of animals and human containing incompletely metabolized after intake, and unintentional discharged wastewaters from pharmaceutical manufacturers and hospitals [3,4]. The widespread antibiotics in the aquatic environment could lead to adverse effects on human and aquatic ecosystem even at trace concentrations, and create reservoirs for bacterial antibiotic resistance and antibiotic resistance genes. Antibiotic resistance genes may directly transmit from animals to humans or conjugated to human pathogens through horizontal gene transfer, thereby increasing the risk of infections for human [5–9]. The abundance and transfer of bacteria carrying antibiotic resistance genes were found to be concomitant with the presence of antibiotics residues, and consequently resulted in the spread of antibiotic resistance genes [10]. Furthermore, coexistence of antibiotics and antibiotic resistance genes can provide favorable conditions for amplifying existing resistance genes and creating novel resistance genes or genomic assemblages [3]. This would accelerate the dissemination of antibiotic-resistant bacteria throughout water ecosystems and thus pose potential human health as well as environmental risks [9]. Therefore, effective removal of antibiotics in water is of great interest and has significant implications for ensuring public and environmental health.

However, traditional wastewater treatment techniques, such as adsorption, biological treatment process, chemical treatments, and membrane filtration, suffer from unavoidable drawbacks of secondary pollution, recalcitrant, and energy or labor intensive, and these

* Corresponding author at: State Key Laboratory of Ore Deposit Geochemistry, Institute of Geochemistry, Chinese Academy of Sciences, Guiyang 550081, China.
** Corresponding author.
E-mail addresses: wanquan@vip.gyig.ac.cn (Q. Wan), antc99@gdut.edu.cn (T. An).

https://doi.org/10.1016/j.apcatb.2021.120734
Received 24 June 2021; Received in revised form 14 September 2021; Accepted 16 September 2021
Available online 20 September 2021

techniques can only partially remove emerging organic contaminants especially for antibiotics [4,11]. Consequently, effectively removing antibiotics from water is a challenge, and extensive efforts have been made to develop new technologies to effectively eliminate antibiotics from water [12]. As an effective and eco-friendly technology for removing antibiotics in water, the advanced oxidation process (AOP) is regarded as a promising alternative to traditional treatment technologies due to the *in situ* generation of high reactivity and low selectivity of reactive oxygen species (ROS) such as hydroxyl and other oxidizing species (including superoxide radicals, sulfate radicals, and chlorine radicals) [13–16]. ROS can react rapidly with most organic compounds, leading to their complete mineralization to nontoxic smaller compounds and even to CO_2 as well as H_2O [17]. As an efficient advanced oxidation process, Fenton reaction has been proved as a promising method for the elimination of antibiotics in the aquatic environment due to its cost-effectiveness, adaptability, and extensive applicability [18]. However, the extensively practical applications of conventional homogeneous Fenton process are still hampered by some drawbacks such as production of large quantities of ferric hydroxide sludge and limited range of optimum pH (usually 2.0–3.5) [14,19].

Heterogeneous Fenton catalysis, which is a combination of surface catalysis at solid-liquid interface and homogeneous catalyzed process by leached/dissolved Fe^{2+}/Fe^{3+} from the solid catalyst, has received increasing attentions and is developed to overcome shortcomings of homogeneous Fenton process [19,20]. Iron bearing minerals like iron (oxyhydr)oxides and iron sulfide minerals are ubiquitous in various Earth surface environments and ore deposits, and commonly served as heterogeneous Fenton catalysts because of their inexpensive, abundant, and environmentally friendly. Among these heterogeneous Fenton catalysts, as the most rich iron sulfide minerals in earth crust, pyrite FeS_2 is regarded as a hopeful material for effectively purifying environmental pollutants due to it can act as both pH regulator for maintaining a low pH required by sustainable Fenton reaction and iron ions source dosage *via* smoothly continuous release of aqueous Fe^{2+} [20,21]. Nonetheless, natural pyrite inevitably contains various large quantities of impurities and even harmful heavy metals as well as metalloids, resulting in its direct application limited by the possible release of potential hazardous ions, which might have a potentially deleterious impact on human and environmental health [22]. In this regard, synthesis of pure-phase pyrite with nontoxicity and high reactivity may be a good choice to address the above problems, and it has attracted considerable interests [23,24].

Numerous studies have been devoted to successfully synthesize micro-nano pyrite crystals with controllable geometrical morphologies, specific facets, and different sizes using various synthetic methods [25,26]. Recently, two-dimensional pyrite nanosheets has attracted considerable attentions due to their higher specific surface area and more

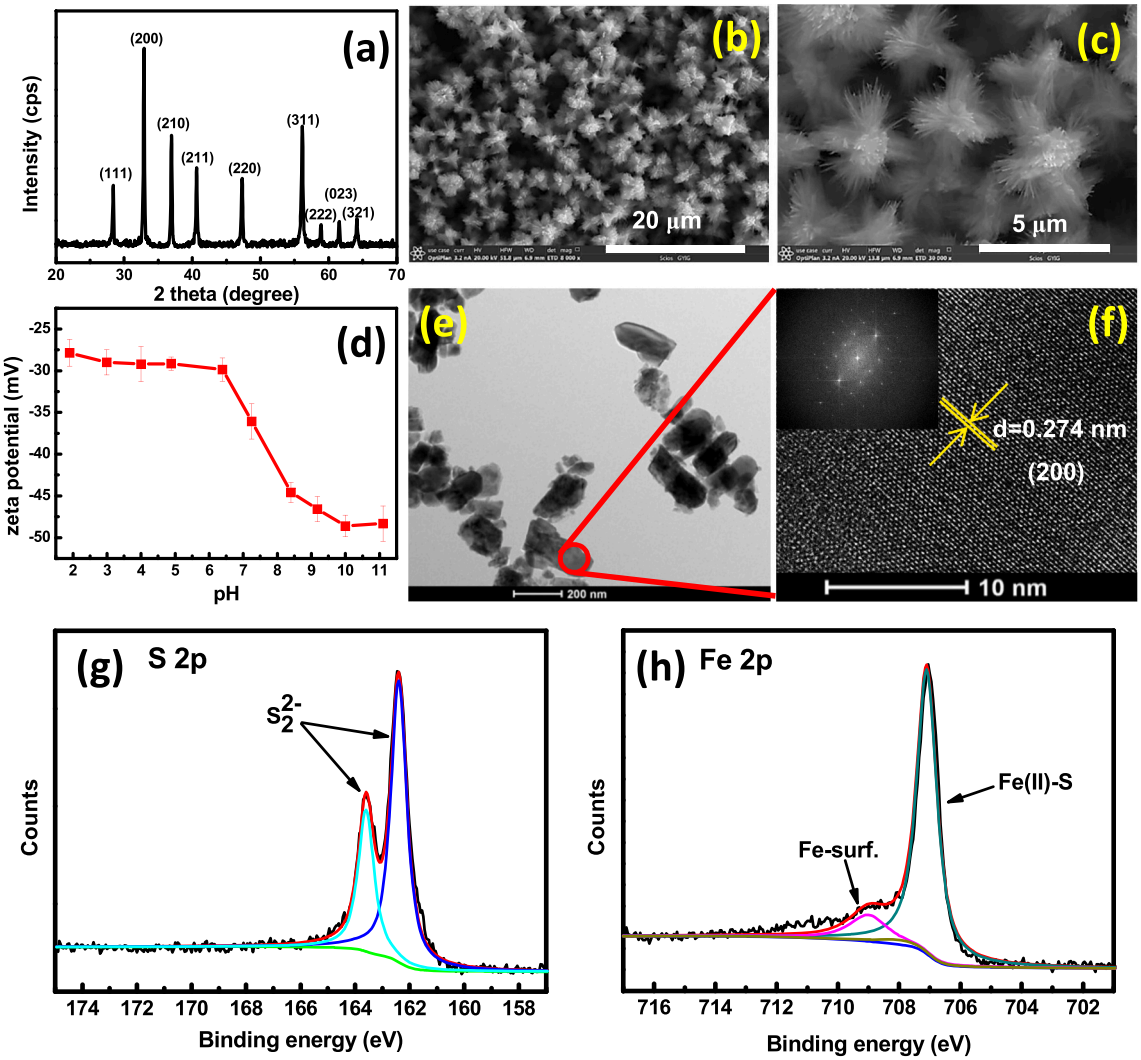

Fig. 1. (**a**) XRD pattern, (**b**) Low-magnification FESEM image, (**c**) high-magnification FESEM image, (**d**) zeta potential values at different pHs, (**e**) Low-magnification TEM image, (**f**) high-magnification TEM (HR-TEM) image with the corresponding fast Fourier transformed (FFT) pattern of lattice fringing pattern, and XPS spectra of S 2p (**g**) and Fe 2p (**h**) for the as-synthesized hexapod-like pyrite nanosheets clusters.

surface active sites compared to their 1D wires, 3D cubes, and bulk counterparts [27,28]. Thus, they might exhibit a better performance for eliminating environmental contaminants *via* adsorption and heterogeneous Fenton catalytic reaction [27,29,30]. Nevertheless, to date, facile synthesis of pyrite nanosheets is still challenging. Most importantly, most of these works regarding pyrite nanosheets are mainly focused on their synthetic methodology, and their application in the highly efficient adsorption and catalytic degradation of antibiotics are still limited. Herein, in this work, a novel heterogeneous Fenton catalyst of hexapod-like ultrathin pyrite nanosheets mineral cluster was synthesized using a facile hydrothermal method with fluoride ion as an agent for capping and shape-controlling for the first time. Ciprofloxacin (CIP) was selected as a model antibiotics to estimate the heterogeneous Fenton catalytic activity of as-prepared pyrite. Influence of water parameters like pH and halide ions on the adsorption and catalytic degradation of CIP was systematically investigated. The dominant ROSs responsible for the CIP degradation and the degradation intermediates during the heterogeneous Fenton process were also identified to understand the catalytic degradation mechanism of CIP. Finally, the potential risks posed by CIP and its degradation products were further estimated. These results indicated that the hexapod-like pyrite nanosheets mineral cluster shows a promising application in sustainable remediation of antibiotics contaminated water.

2. Experimental section

2.1. Synthesis and characterization of hexapod-like pyrite nanosheets mineral cluster catalyst

In a typical process, 0.015 mol of $FeSO_4{\cdot}7H_2O$ was first mixed in water (20 mL) at room temperature. Then $Na_2S{\cdot}9H_2O$ (0.015 mol) and S (0.015 mol) were dissolved into water (20 mL) and then heated until the solution became transparent, which was subsequently added dropwise to the above suspension under vigorous stirring for 10 min. Then 0.326 g NaF was added into above suspension, and the pH of suspension was adjusted to 4.0. Then the suspension was transferred into Teflon-line autoclave (100 mL), and hydrothermally treated at 120 °C for 24 h. After hydrothermal reaction, the resultant black product was centrifuged to harvest, and fully washed with water, Na_2S boiling solution (1 mol/L), HCl (1 mol/L), and absolute ethanol for several times. Finally, the as-synthesized sample was dried at 30 °C and then stored in an anaerobic environment. Deoxygenated deionized water was used in all experiments. The crystal phase composition and crystallinity were characterized using X-ray diffraction (XRD, Empyrean, PANalytical B.V, Netherlands) operating with Cu-Kα radiation. The elemental composition was characterized using X-ray photoelectron spectroscopy (XPS, Thermo Fisher K-Alpha, USA) with monochromated Al Kα (1486.6 eV) source operated at 110 W and the C 1s peak at 284.8 eV was employed to calibrate XPS spectra. Sample morphologies were observed using transmission electron microscope (TEM, Tecnai G2 F20 S-Twin, FEI Company, Hillsboro, OR, USA) and Field emission scanning electron microscopy (FESEM, Scios, FEI Company, USA) with an acceleration voltage of 30.0 kV. The BET (Brunauer–Emmett–Teller) model was used to analyze the specific surface area by a nitrogen adsorption apparatus (Autosorb-iQ2-MP, Quantachrome). The zeta potentials of samples were measured with electrophoretic effect using a multi angle particle size and high sensitive zeta potential analyzer (Omni, Brookhaven, USA).

2.2. Adsorption and catalytic degradation experiments of CIP

CIP was chosen to determine heterogeneous Fenton activity of as-prepared pyrite. Reaction solution was operated at room temperature and stirred throughout the experiment with a magnetic stirrer. In a typical adsorption experiment, pyrite (0.1 g) was first added into solution (100 mL) containing CIP with various concentrations and initial pH. Degradation experiment was performed in the same reactor under identical conditions. After 10 min adsorption of CIP by pyrite, H_2O_2 solution (2 mL, 100 mmol/L) was added into above 20 ppm CIP solution to trigger Fenton reaction. About 3 mL of solution was sampled at different time intervals and filtered with 0.45 mm Millipore filter for further analysis. The CIP concentrations were analyzed by HPLC (high pressure liquid chromatography, Agilent 1200) at the wavelength of 278 nm with a dual absorbance detector (DAD) detector equipped with a Kromasil ODS (5 μm, 4.6 mm × 150 mm) reverse-phase column. HPLC tandem mass spectrometry (HPLC/MS/MS, Q Exactive, ThermoFisher Scientific, USA) was used to identify intermediates. The detailed information is provided in the Supporting information. The data displayed in this work were the average values obtained from experiments replicated in triplicate.

3. Results and discussion

3.1. Structure and morphology properties of prepared hexapod-like pyrite nanosheets mineral cluster catalyst

Fig. 1a demonstrates dominant characteristic diffraction peaks of XRD patterns for the as-synthesized sample. The diffraction peaks at $2\theta = 28.51°$, 33.08°, 37.11°, 40.78°, 47.41°, 56.28°, 59.02°, 61.69°, and 64.28° were well attributed to the (111), (200), (210), (211), (220), (311), (222), (023), and (321) planes of cubic pyrite (FeS_2) (JCPDS card no. 42-1340) with a space group of $Pa\bar{3}$, respectively [25]. Pyrite (FeS_2) was found to be the only crystalline phase. The characteristic diffraction peaks were sharp, suggesting a good crystallinity of the as-synthesized sample [25]. Typical FESEM images (Fig. 1b and c) demonstrate orthogonal hexapod-like nanosheets clusters with good uniformity, in which the nanosheets were oriented into a hexapod, and each pod had a length in the range of approximately 1–3 μm. The average thickness of pyrite nanosheets was about 10 nm or less. The arrangement of pyrite nanosheets was highly directional, in which nanosheets grew mainly along three orthogonal directions, implying preferential growth along specific crystallographic directions [31]. The specific surface area of the hexapod-like pyrite nanosheet clusters was 6.63 m^2/g. The low-magnification TEM image (Fig. 1e) shows the width of the individual nanosheets was about 100 nm. The HRTEM image (Fig. 1f) recorded from the yellow circled area in Fig. 1e indicates a well-crystalline nature with a lattice fringes spacing of *ca.* 0.274 nm, which is assigned to (200) crystallographic interplanar distances of pyrite FeS_2. The zone axis of these nanosheets is [001], which confirms that they are terminated with {100} facets. The continuous lattice fringes in whole nanosheet region reveal that each pyrite nanosheet has a perfect single crystalline structure, which is consistent with the two-dimensional spot array in the FFT pattern (upper left inset in Fig. 1f) of its corresponding HRTEM image. The result is consistent with the cubic structure observed in XRD, and it suggests that hexapod-like pyrite nanosheets mineral clusters formed and grew along the six equivalent <001> directions [31]. The EDX result (Fig. S1) further confirmed that the as-synthesized the hexapod-like pyrite nanosheets mineral clusters was composed of S and Fe elements with a molar ratio of S/Fe of ~ 2. Fig. 1g and h shows the XPS spectrometry of S 2p and Fe 2p. The S 2p bands could be fitted with the doublets at 162.4 and 163.6 eV. The peak at 162.4 eV corresponds to S_2^{2-} in pyrite. The peak at 163.6 eV is associated with polysulfide species (S_2^{2-}) [32,33]. The Fe 2p peak at 707.2 eV is assigned to Fe^{2+} in pyrite. The peak at 709 eV could be attributed to Fe surface states of Fe-surf, which can be interpreted to be high-spin Fe^{2+} surface ions with unpaired electrons in the valence band [34,35]. These results confirm successful synthesis of that the prepared product was pure pyrite (FeS_2).

Fig. 1d illustrates the zeta potential values of the as-synthesized pyrite at different pHs. The results show the zeta potential values of pyrite were negative when pH values ranged from 2 to 11, indicating that pyrite is negatively charged at all tested pH conditions because the

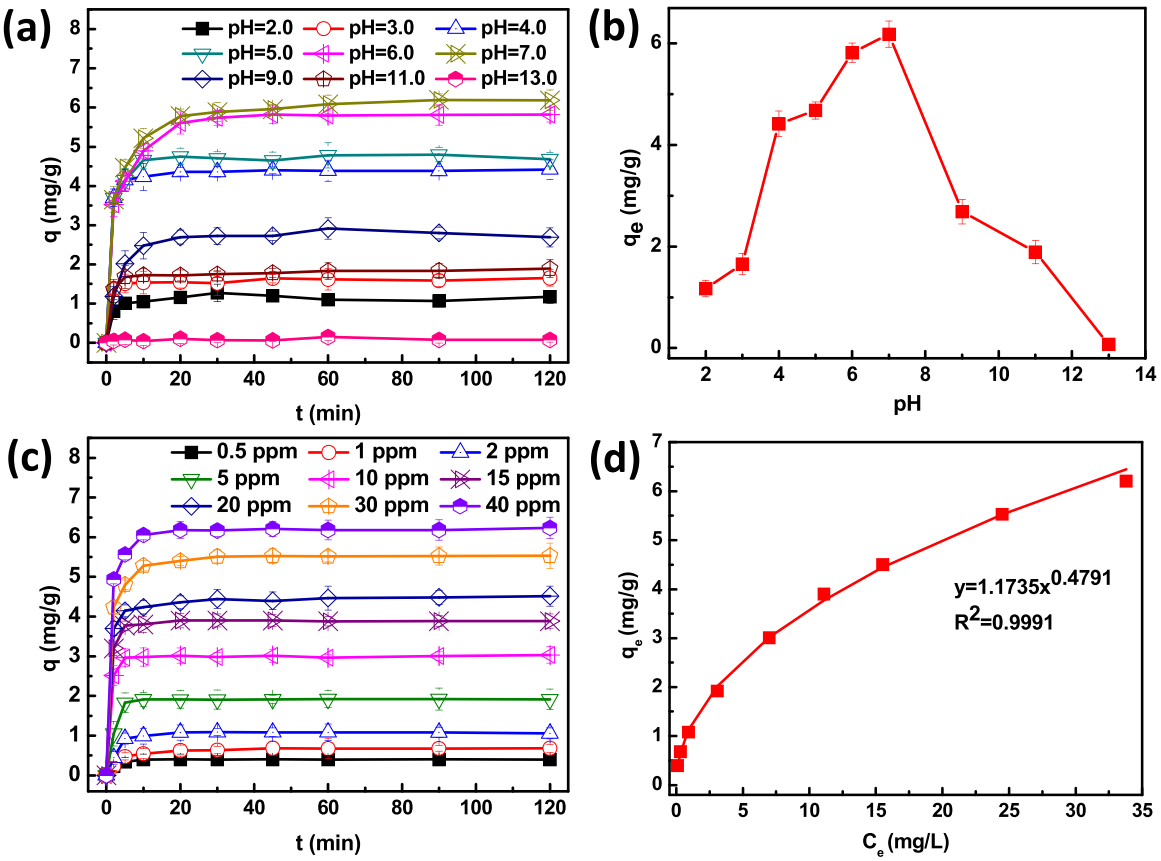

Fig. 2. (**a**) Effect of pH on adsorption of CIP (20 ppm); (**b**) The equilibrium adsorption amount (q_e) of CIP at different pHs; (**c**) Adsorption of different CIP concentrations at pH = 4; (**d**) Fitting of adsorption isotherms of CIP through Freundlich models.

surface functional groups are predominantly negatively-charged. This can be ascribed to the presence of different types of surface functional groups, including ≡S–H, ≡S–OH, and ≡Fe–OH, on the pyrite surface through coordination with water. These amphoteric surface groups are primarily responsible for the surface charge characteristics. Deprotonation of these chemical functional groups would yield negatively charged surface sites, and the surface charge density increases with increasing solution pH [36].

3.2. Adsorption of CIP by the hexapod-like pyrite nanosheets mineral clusters

Adsorption capability of CIP onto the hexapod-like pyrite nanosheets mineral clusters was further performed. Solution pH often influences the transport and fate of ionizable organic contaminants since they have ionizable functional groups at different pHs. Hence, the effect of pH was systematically investigated. Fig. 2a shows that CIP was rapidly absorbed by the hexapod-like pyrite nanosheets mineral clusters and reached adsorption equilibrium within 10–20 min at all tested pH conditions, indicating that the hexapod-like pyrite nanosheets mineral clusters possess high adsorption ability. The adsorption of CIP was highly pH dependent, and similar adsorption kinetic curves were observed for different pHs. The equilibrium adsorption amount (q_e) of CIP (Fig. 2b) initially increased with pH value increased from 2.0 to 7.0 and reached a maximum at about pH 7.0 and then remarkably decreased at higher pH values. When the pH value increased to 13, negligible adsorption of CIP was observed. Maximum adsorption capacities of CIP (about 6.11 mg/g) were obtained at pH 7. Since the pH isoelectric point (pH_{iep}) for pyrite was lower than 2.0, the increasing pH also resulted in a greater extent of deprotonation of surface groups and thus more negative charges on the pyrite surface. CIP is an amphoteric molecule, which contains one acidic and one basic group, and the pK_a of these groups is 6.16 and 8.23, respectively [37]. Different dissociation species would be existed at different solution pHs, including positively charged ($HCIP^+$), zwitterionic ($CIP^{\pm}$), and negatively charged (CIP^-) species (Fig. S2). With increasing pH, deprotonated species become more dominant due to hydrolysis of CIP. At low pH values, the favored hydrogen ion adsorption on pyrite surface would lead to the decreased adsorption of CIP. At high pH values, both the anionic carboxylate group of CIP and the surface sites of pyrite are significantly negative charged, resulting in an electrostatic repulsion between them and low equilibrium adsorption amount of CIP. At pH = 7.0, zwitterions of $CIP^{\pm}$ is the dominant dissociation species of CIP, and thus adsorption efficiency reached the highest. This can be explained by the weakened electrostatic interaction and enhanced hydrophobic interaction due to the higher hydrophobicity of zwitterionic CIP [38,39]. Moreover, the solubility of different CIP species is highly pH dependent, and the zwitterionic $CIP^{\pm}$ has the lowest solubility and the highest hydrophobicity at pH around 7, and the hydrophobic interaction for zwitterionic CIP sorption on pyrite would be enhanced [40,41]. The electrostatic attraction, hydrophobic interaction, and van der Waals interactions between CIP and pyrite surface controls the adsorption process, and the cumulative effect of these features will determine the optimum pH for adsorption. The adsorption isotherm of CIP on pyrite at pH 4.0 was investigated with different initial concentrations of CIP (Fig. 2c). The equilibrium adsorption amount of CIP gradually increased with increasing initial concentrations of CIP. The adsorption data could be fitted reasonably well to Freundlich model with a high regression coefficient R^2 value (0.9991) (Fig. 2d), suggesting a multilayer adsorption feature of CIP on heterogeneous energy distribution of the sorption sites on pyrite surface [42]. This could be attributed to that the simultaneous possession positively and negatively charged groups of CIP facilitates their multilayer adsorption [43]. This

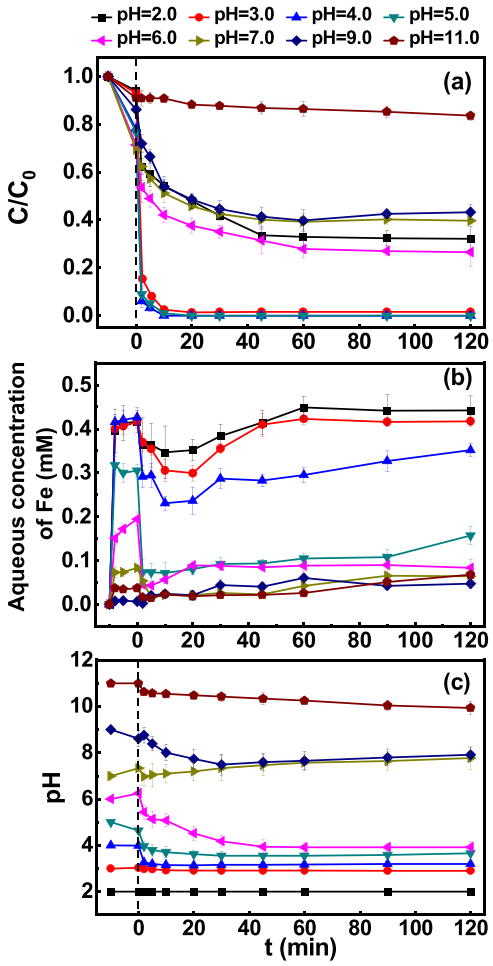

Fig. 3. Effect of different initial pHs on (**a**) the degradation of CIP, (**b**) the aqueous concentrations of Fe, and (**c**) the changes in the solution pH during the Heterogeneous Fenton catalytic reaction process by the hexapod-like pyrite nanosheets clusters. Experimental conditions: pyrite = 1 g/L, CIP = 20 mg/L, H_2O_2 = 2 mmol/L.

result could also be used to reasonably explain that the zwitterionic $CIP^{\pm}$ under neutral conditions are more likely to be adsorbed on the surface of pyrite, and thus maximizing the adsorption capacity.

3.3. Heterogeneous Fenton catalytic degradation of CIP by hexapod-like pyrite nanosheets mineral clusters

Solution initial pH has a decisive influence on the Fenton reaction process [1]. To ascertain the optimum Fenton catalytic degradation conditions for CIP by hexapod-like pyrite nanosheets mineral clusters, we first investigated the effect of solution initial pH (2.0–11.0) on the Fenton catalytic degradation of CIP (Fig. 3a). The experiments were carried out in system containing CIP (20 mg/L), pyrite (1 g/L) and H_2O_2 (2 mM) at different initial pH. As shown, CIP degradation clearly became quicker with the increase of pH from 2.0 to 3.0. When the solution initial pH was within 3.0–5.0, CIP could be quickly degraded. The highest degradation rate of CIP was achieved at initial pH 4.0, and CIP could be completely degraded within 10 min. Further increasing the solution initial pH, a remarkably decreased CIP degradation rate could be found. As solution initial pH value increased to 11.0, only ~ 10% CIP was removed within 120 min, and the decreased CIP concentration was due to their adsorption on hexapod-like pyrite nanosheets mineral clusters, indicating a negligible degradation efficiency.

At high pH values, hydrogen peroxide is preferentially decomposed into H_2O and O_2 without generating hydroxyl radicals (•OH),

$$(OH^- + H_2O_2 \leftrightarrow HO_2^- + H_2O) \quad (1)$$

$$HO_2^- + H_2O_2 \leftrightarrow O_2 + H_2O + OH^- \quad (2)$$

which leads to a decrease in the production of •OH [1]. At the pH range of 2.0–4.0, the dominant species of ferrous is $Fe(OH)^+$ complex, which has a higher activity than free Fe^{2+} in Fenton reactions. However, a strong acidic condition especially pH lower than 2.5 may hinder the regeneration of Fe^{2+} through reactions of pyrite with Fe^{3+} and enhance the formation of $[FeOH]^{2+}$ and $[Fe(H_2O)]^{2+}$ complex, which have lower reaction rate with H_2O_2 and will produce lower amounts of •OH [44,45]. Furthermore, •OH and Fe^{2+} will also be consumed by the abundant H^+ as a radical scavenger,

$$•OH + H^+ + Fe^{2+} \rightarrow H_2O + Fe^{3+} \quad (3)$$

reducing the production of •OH, thus decreasing the CIP removal efficiencies [46].

In addition, the decreased CIP removal with increasing solution initial pH may be ascribed to decreasing Fe solubility and variation of pyrite surface characteristics [47]. Thus, the aqueous concentrations of Fe as a function of stirring time for suspensions with different initial pHs during the Fenton reaction process were measured (Fig. 3b). In the absence of H_2O_2, the concentrations of dissolved Fe decreased with increasing initial pH of suspension. Dissolved Fe could be detected in the solution, suggesting the dissolution of Fe from pyrite surface [47]. Specifically, concentrations of dissolved Fe with initial pHs ranged from 2.0 to 4.0 were remarkably higher, reaching about 0.42, 0.42, and 0.43 mM after stirring for 10 min with initial pH 2.0, 3.0, and 4.0, respectively. This indicates that acidic pH facilitates the dissolution of Fe^{2+} from pyrite. A decrease in Fe concentration in solution with rising solution initial pH would reduce the generation of solution phase •OH, which is well consistent with the decreased removal of CIP with increasing initial pH of suspension [47]. The solubility for Fe species (including Fe^{2+} and Fe^{3+}) decreased with increasing solution pH, resulting in accumulating and precipitating Fe^{2+}/Fe^{3+}-(oxy)-hydroxides (such as $Fe(OH)_2$, goethite and ferrihydrite) on pyrite surface and in solution *via* Fenton reaction [48,49]. These precipitations would consume the ferrous ions and inhibited the Fenton reaction, leading to the significant decrease of CIP removal. Once H_2O_2 was added to the system, the concentration of dissolved Fe was decreased swiftly at initial 10 min, followed by a more gradual increase. This could be attributed to the transformation of dissolved Fe species (especially Fe^{3+}) to Fe-oxides which have lower solubility. This could be confirmed by the SEM image (Fig. S3) in which the pyrite nanosheets were became shorter and thicker after 120 min Fenton reaction. With the consumption of H_2O_2, the aqueous concentrations of Fe increased gradually because of the dissolution of Fe from pyrite surface.

Pyrite can not only introduce dissolved Fe into the solution, but it can also increase the H^+ concentration or reduce the pH of solution through following Eqs. (4)–(6). H_2O_2 would react with the pyrite surface to release Fe^{3+} into solution, and Fe^{3+} could re-oxidize the pyrite surface to generate Fe^{2+} in solution [47]. Solution pH also contributes to the speciation of aqueous Fe and the production of •OH [50]. These two functions will be favorable for the Fenton reaction [1]. Therefore, the corresponding change in the solution pH during Fenton reaction was studied systematically. Fig. 3c demonstrates a drop tendency in solution pH with the Fenton reaction proceeding, confirming that pyrite could decrease solution pH through reaction with H_2O_2, oxygen, as well as Fe^{3+}. Specifically, the pH of the suspension with an initial pH of 2.0, 3.0, 4.0, 5.0, 6.0, 9.0, and 11.0 dropped to 1.99, 2.91, 3.16, 3.55, 4.18, 7.49, and 10.43 after adding H_2O_2 for 30 min, respectively. However, the precipitation of Fe^{2+}/Fe^{3+}-(oxy)-hydroxides may affect the reaction between Fe^{3+} and pyrite, which would decrease the rate of pH drop with the increase in solution initial pH. The precipitates could also block the surface of pyrite and hinder further oxidation reactions, while the

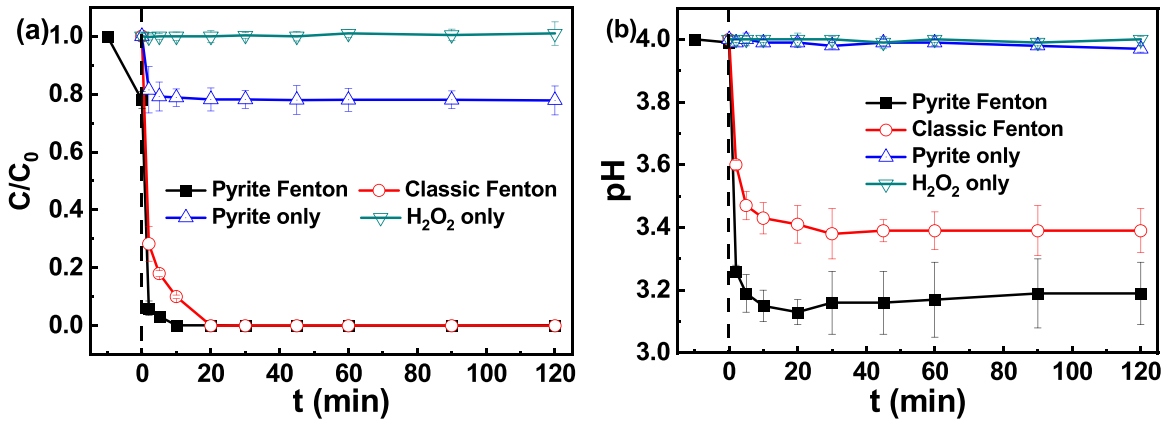

Fig. 4. Degradation of CIP (**a**) and the changes in the solution pH (**b**) in various reaction systems at initial pH = 4: heterogeneous Fenton by the hexapod-like pyrite nanosheets clusters, classic Fenton, pyrite alone, and H_2O_2 alone.

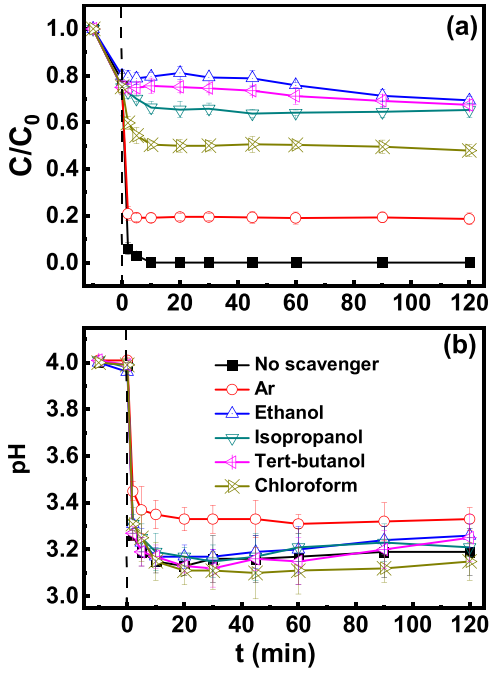

Fig. 5. The heterogeneous Fenton catalytic degradation of CIP **(a)** and the changes in the solution pH **(b)** during the Heterogeneous Fenton reaction process at initial pH = 4 by the hexapod-like pyrite nanosheets clusters with different scavengers (50 mmol/L).

degradation rate of CIP became concomitantly slower [45].

$$2FeS_2 + 7O_2 + 2H_2O \rightarrow 2Fe^{2+} + 4SO_4^{2-} + 4H^+ \quad (4)$$

$$2FeS_2 + 15H_2O_2 \rightarrow 2Fe^{3+} + 4SO_4^{2-} + 2H^+ + 14H_2O \quad (5)$$

$$FeS_2 + 14Fe^{3+} + 8H_2O \rightarrow 15Fe^{2+} + 2SO_4^{2-} + 16H^+ \quad (6)$$

Fig. 4a shows the changes in CIP concentrations and pH in various reaction systems, including pyrite Fenton, classic Fenton (containing 0.45 mM $FeSO_4$), pyrite alone, and H_2O_2 alone. CIP concentration remained unchanged within 120 min under H_2O_2 alone (without pyrite), suggesting no considerable CIP degradation by H_2O_2. Additionally, a 20% reduction in CIP concentration in pyrite alone (without H_2O_2) system is due to the adsorption as demonstrated above. Complete CIP degradation was achieved within 20 min in classical homogeneous Fenton system. Comparatively, CIP degradation in pyrite Fenton system was much more efficient than classical homogeneous Fenton system, and full degradation of CIP would be achieved only within 10 min, indicating a higher catalytic activity of pyrite Fenton system. The enhanced removal of CIP in pyrite Fenton system should be attributed to adsorption effect of pyrite to CIP. Moreover, simultaneous availability of suitable pH (Fig. 4b) and continuous release of aqueous Fe^{2+} from pyrite also facilitate the quick and complete catalytic degradation of CIP [45, 50].

3.4. Contribution of ROSs

To investigate contribution of ROSs to pyrite Fenton degradation of CIP, quenching experiments were conducted by adding individual scavengers to remove the respective ROSs in pyrite Fenton system. Isopropanol was used to scavenge $^{\bullet}OH_{bulk}$ ($^{\bullet}OH$ in solution), tert-butanol was used to remove total $^{\bullet}OH$ ($^{\bullet}OH$ in solution and $^{\bullet}OH$ adsorbed on the surface of pyrite), chloroform was used to scavenge $O_2^{\bullet-}$, ethanol was employed to scavenge all ROSs, and Ar was employed to exclude O_2 [45, 51]. As Fig. 5 shows, without addition of any scavengers, more quick degradation of CIP was found, the complete degradation of CIP could be achieved only within 10 min. However, the degradation of CIP was obviously inhibited in the presence of these scavengers. When ethanol was added, except for the adsorption (~ 20%), only slightly reducing CIP concentration was found, indicating that ROSs play a primary role in pyrite Fenton system. The addition of tert-butanol and isopropanol remarkably hindered the degradation of CIP, and only approximately 25% and 35% decrease in the CIP concentration was achieved after 20 min, respectively. Results suggest that CIP degradation is predominantly attributed to the $^{\bullet}OH_{bulk}$, and $^{\bullet}OH_{ads}$ ($^{\bullet}OH$ adsorbed on pyrite surface) also plays a minor role, proving that the adsorption of CIP on pyrite can enhance its removal efficiencies to a certain degree through a series of heterogeneous reactions [1,45,52]. The addition of chloroform could also reduce degradation of CIP with 50% decrease in CIP concentration after 20 min. $O_2^{\bullet-}$ is a weak reductant ($E^{\circ}(O_2/O_2^{\bullet-}) = -0.16$ V), which is not sufficiently strong to degrade CIP, thus it plays an indirect role in pyrite Fenton degradation of CIP through the transformation of $O_2^{\bullet-}$ to •OH.

$$O_2^{\bullet-} + H_2O_2 \rightarrow \bullet OH + OH^- + O_2 \quad (7)$$

To further discriminate whether $O_2^{\bullet-}$ was generated from H_2O_2 or dissolved O_2, Ar was aerated in solution to exclude O_2 to eliminate $O_2^{\bullet-}$ produced by oxidation of Fe^{2+} released from pyrite,

$$Fe(II) + O_2 \rightarrow Fe(III) + O_2^{\bullet-}, \quad (8)$$

and 80% decrease of CIP concentration was found after 20 min, demonstrating that $O_2^{\bullet-}$ generated from O_2 also plays a non-negligible role during the degradation process of CIP. In summary, in this pyrite

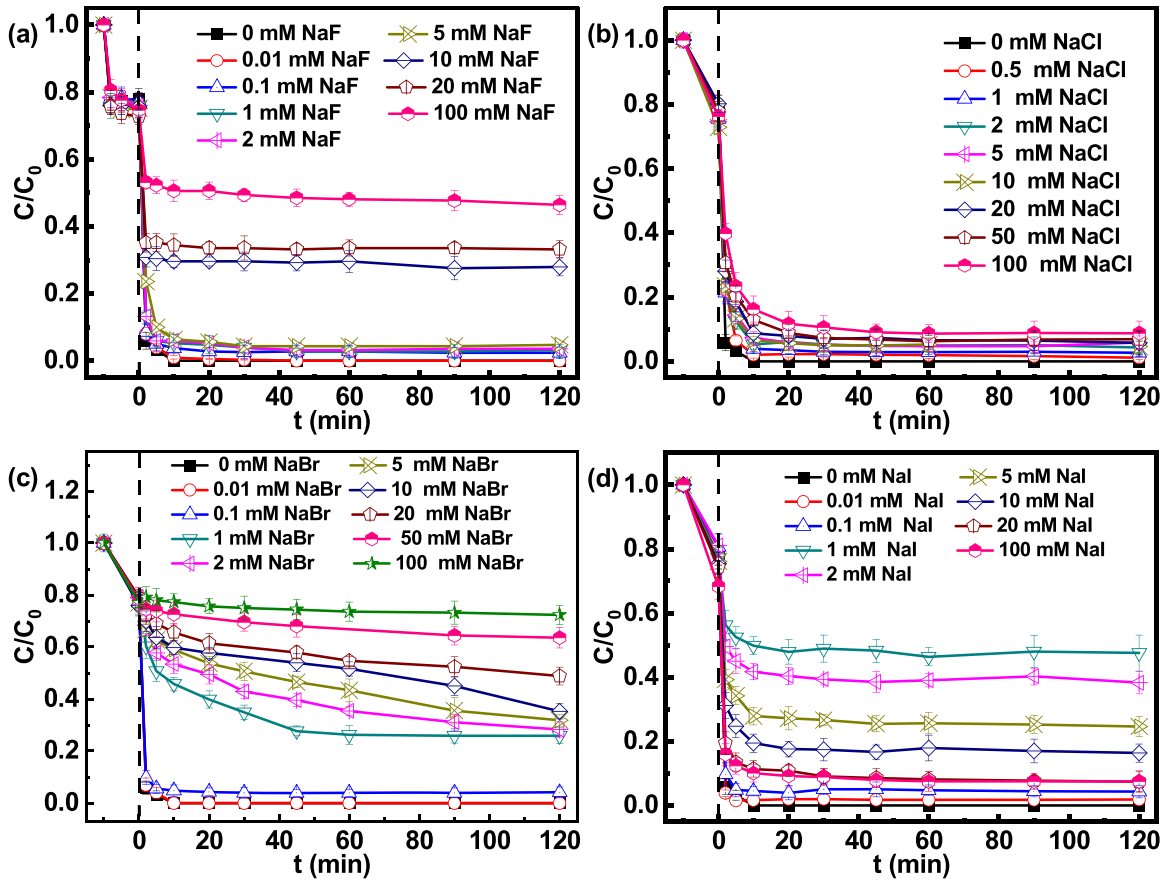

Fig. 6. The heterogeneous Fenton catalytic degradation of CIP by the hexapod-like pyrite nanosheets clusters at initial pH= 4 with different concentrations of NaF (**a**), NaCl (**b**), NaBr (**c**), and NaI (**d**).

Fenton system, CIP was directly oxidized and decomposed by $^{\bullet}OH$, which was the dominant ROSs responsible for the CIP degradation, and it can be produced through Fenton reaction

$$Fe(II) + H_2O_2 \rightarrow Fe(III) + OH^- + {}^{\bullet}OH \quad (9)$$

and transformation from $O_2^{\bullet-}$. While $O_2^{\bullet-}$ generated from H_2O_2 or dissolved O_2 was also an important contributor to the CIP degradation *via* formation its derivatives $^{\bullet}OH$. This is consistent with the results of photocatalytic degradation of fluoroquinolone pharmaceutical compounds by TiO_2 that $^{\bullet}OH$ was also the primary ROSs, and it would be an efficiently alternative treatment technology for removal of refractory organic pollutants in aqueous environment [53–55].

3.5. *Effect of halide ions on the degradation process of CIP*

The universal occurrence of halide ions in estuarine and coastal waters is of great importance to affect transport and fate of contaminants [56]. For thorough understanding of the influence of halide ions on pyrite Fenton degradation process of CIP, various frequently used halides (NaF, NaCl, NaBr, and NaI) were added into the solution with a series of concentrations.

With added NaF concentration ranging from 0 to 5 mM, only a slight decrease of CIP degradation efficiencies was observed (Fig. 6a). As the concentration of NaF was increased, the degradation efficiencies of CIP were decreased. When NaF concentration was increased up to 10 mM, the degradation efficiencies of CIP were significantly decreased. When NaF concentrations were increased to 10, 20, and 100 mM, approximately only 72%, 67%, and 54% of CIP was removed after 120 min, respectively. This indicates an inhibitory effect of NaF on the pyrite Fenton degradation process of CIP when NaF concentration was above 10 mM. At the same time, the pH of the suspension increased with NaF concentration increasing from 0 to 5 mM and then remarkably decreased at higher NaF concentration, implying a higher pH buffering effect with a higher NaF concentration. It is worth noting that the pH of the suspension was higher than initial value of 4.0 after adsorption for 10 min when NaF concentration exceeded 2 mM (Fig. S4a). This can be attributed to the ion exchange reaction between fluoride and ≡Fe–OH on the surface of pyrite releases OH^- into the solution.

$$\equiv Fe\text{-}OH + F^- \rightarrow \equiv Fe\text{-}F + OH^- \quad (10)$$

Due to the very high affinity of ferric ion for fluoride, the inhibition effect by higher concentration of NaF may be attributed to the coordination of fluoride to dissolved Fe(III) to generate insoluble salts and less reactive complex ($(Fe(III)F)^{2+}$, $(Fe(III)F_2)^{+}$, and $(Fe(III)F_3)^{0}$), which is catalytically inactive in the Fenton reaction [18,57].

The addition of NaCl did not show obvious effects on CIP removal (Fig. 6b). The degradation rate decreased slightly with rising NaCl concentration, but the degradation rate could reach ~ 90% even with the addition of 100 mM NaCl within 20 min. Furthermore, the pH of the suspension remarkably increased with NaCl concentration increasing from 0 to 100 mM, implying release of OH^- during the reaction process (Fig. S4b). Comparatively, the addition of NaBr (Fig. 6c) or NaI (Fig. 6d) could significantly decrease degradation efficiencies of CIP, and the inhibition effect of Fenton reactions by NaBr or NaI was noticeable when the added [NaBr] or [NaI] ≥ 1 mM. At low concentration (1–5 mM), NaI suppressed the degradation of CIP more efficiently than NaBr. However, at a high concentration (≥ 10 mM), the inhibition effect of CIP degradation by NaI was lower than NaBr. For the system of NaBr addition, the inhibition effect exhibited a monodirectional increase tendency with NaBr concentration. With increase of NaBr concentration from 0 to

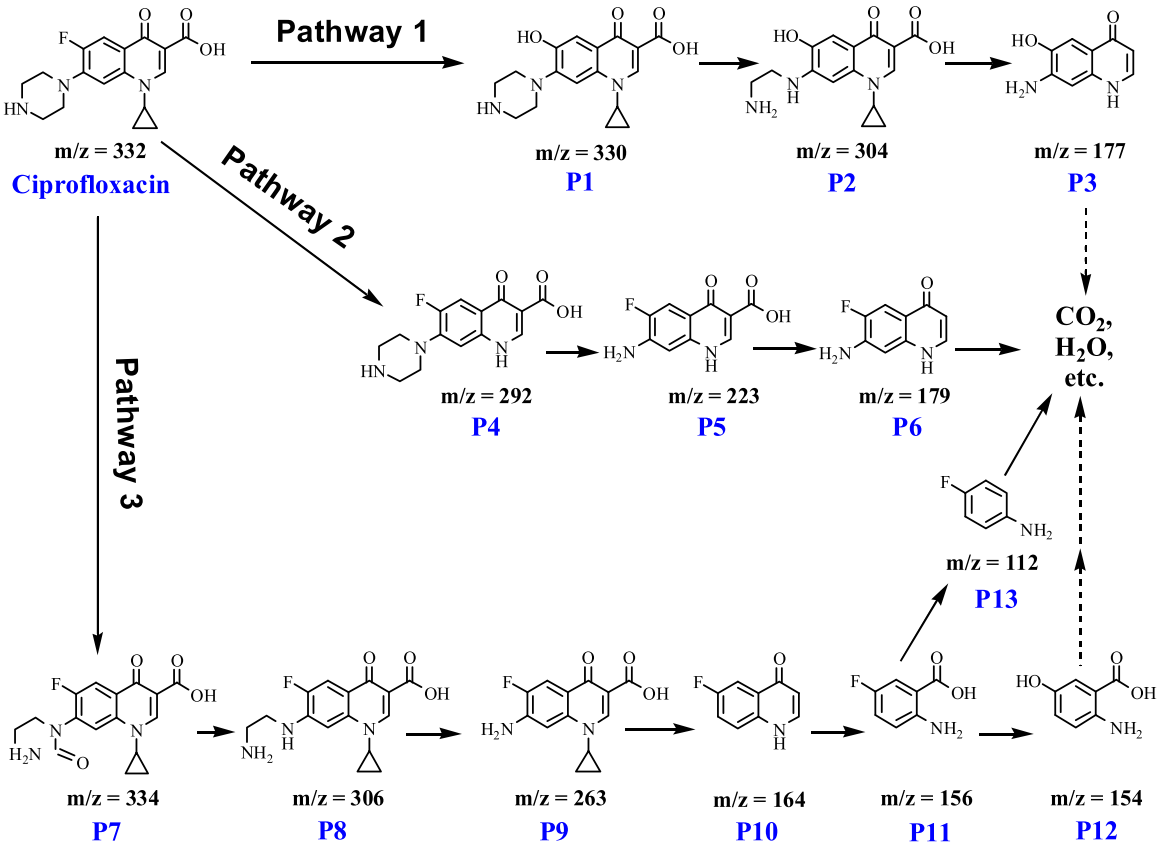

Scheme 1. Possible catalytic degradation pathways of CIP in Fenton system by the hexapod-like pyrite nanosheets clusters.

1 mM, degradation efficiencies of CIP decreased significantly. When NaBr concentration increased to 100 mM, only ~ 28% decrease of CIP was obtained within 120 min, indicating that degradation of CIP could be almost completely suppressed due to ~ 20% CIP was adsorbed by pyrite. Notably, for the system of NaI addition, the lowest degradation efficiency of CIP was observed with addition of 1 mM NaI, in which only ~ 52% decrease of CIP was obtained within 120 min. Further increasing NaI concentration, degradation efficiencies of CIP increased steadily. pH of the suspension with the addition of NaBr (Fig. S4c) or NaI (Fig. S4d) also monodirectionally increased similar to the system with the addition of NaCl.

According to the results of reactive species analysis, $^{\bullet}OH$ is mainly responsible for the degradation of CIP when halides are not added. The reduction in degradation efficiencies in the presence of halide ions indicates that the type and contribution of the main reactive oxidant for CIP degradation might be altered. This may be attributed to that $^{\bullet}OH$ could be scavenged by Cl^-, Br^-, and I^- to form lower oxidation power species of halide radicals ($X^{\bullet}$, such as $Cl^{\bullet}$, $Br^{\bullet}$, and $I^{\bullet}$) than $^{\bullet}OH$ (2.80 V) through the following reaction (Eqs. (11), (12)). These trends are in reasonable agreement with the phenomenon that the suspension pH increased with the increase of halide concentration. In the presence of a high concentration halide ions, the excessive halide ions would further react with $X^{\bullet}$ to generate much less reactive and more selective dihalide radical anions ($X_2^{\bullet-}$, such as $Cl_2^{\bullet-}$, $Br_2^{\bullet-}$, and $I_2^{\bullet-}$) than $X^{\bullet}$ at initiating the degradation of organic compounds, thus degradation of CIP can be significantly suppressed [56,58–62]. However, CIP removal was slightly inhibited with the addition of NaCl. This can be interpreted as that the predominant reactive oxidant of $Cl^{\bullet}$ ($E^0[Cl^{\bullet}/Cl^-] = +2.55$ V) and $Cl_2^{\bullet-}$ ($E^0[Cl_2^{\bullet-}/Cl^-] = +2.13$ V) are highly reactive in transforming a variety of organic compounds, thus CIP could be readily and rapidly degraded by them. The remarkable inhibition of CIP degradation by Br^- and I^- is mainly due to formation of the less-reactive $Br^{\bullet}$ ($E^0[Br^{\bullet}/Br^-] = +1.94$ V), $I^{\bullet}$ ($E^0[I^{\bullet}/I^-] = +1.33$ V), $Br_2^{\bullet-}$ ($E^0[Br_2^{\bullet-}/Br^-] = +1.66$ V), and $I_2^{\bullet-}$ ($E^0[I_2^{\bullet-}/I^-] = +1.03$ V), which could not react with CIP [60,63]. Furthermore, H_2O_2 can also react with excess I^- to produce I_2 and I_3^- through Eqs. (13), (14). Increasing I^- concentration could also enhance the solubility of I_2 and the stability of I_3^- generated in aqueous solution. Therefore, the gradually increased degradation efficiencies of CIP when [NaI] > 1 mM are associated with the enhanced production of I_2, coexisting I_3^-, $I^{\bullet}$ and $I_2^{\bullet-}$ [64,65]. Additionally, the reduction of catalytic degradation efficiencies of CIP in the presence of halide ions may be caused by competition between CIP and halide ions for the active site on pyrite surface [63].

$$\bullet OH + X^- \leftrightarrow ClOH^{\bullet-} \leftrightarrow X\bullet + OH^- \quad (11)$$

$$X\bullet + X^- \leftrightarrow X_2^{\bullet-} \quad (12)$$

$$2I^- + H_2O_2 + 2H^+ \leftrightarrow ClOH^{\bullet-} \leftrightarrow I_2 + 2H_2O \quad (13)$$

$$I_2 + I^- \leftrightarrow I_3^- \quad (14)$$

3.6. Intermediate identification and catalytic degradation mechanism of CIP

The degradation intermediates of CIP in pyrite Fenton system were identified using HPLC/MS/MS. Thirteen significant intermediates generated from the degradation process were qualitatively detected and identified. The detailed data of intermediates (such as molecule weight, and structures) and three possible degradation pathways for CIP were tentatively proposed (Scheme 1). The substitution of the F atom with $^{\bullet}OH$ to produce intermediate P1 ($m/z = 330$) could occur through pathway 1. The cleavage and loss of piperazine ring, cyclopropyl group and carboxylate group of the quinolone ring from P1 formed intermediate P2 ($m/z = 304$) and P3 ($m/z = 177$). Pathway 2 indicates oxidation of cyclopropyl group resulting in the ring cleavage to form P4 ($m/$

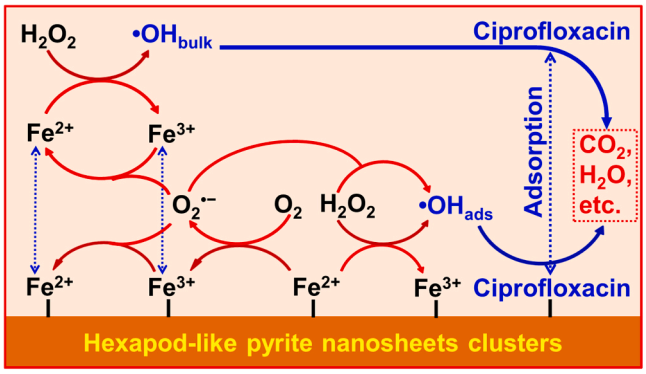

Scheme 2. Adsorption and Fenton catalytic degradation mechanism of ciprofloxacin by the hexapod-like pyrite nanosheets clusters.

$z = 292$), which was further degraded with the loss of the piperazine ring (P5, $m/z = 223$) and carboxylate group of the quinolone ring (P6, $m/z = 179$). The cleavage and loss of piperazine ring of CIP could take place through the rout CIP→P7 ($m/z = 334$)→P8 ($m/z = 306$)→P9 ($m/z = 263$) in pathway 3, and subsequent loss of amino group, cyclopropyl group, and cyclopropyl group yielded P10 ($m/z = 164$) [66,67]. P10 was additionally changed to P11 ($m/z = 156$) by the cleavage of quinolone ring, which subsequently converted to form P12 ($m/z = 154$) through the substitution of the F atom with a $^{\bullet}$OH or P13 ($m/z = 112$) through decarboxylation. In these pathways, pathways 2 and 3 are the most prevalent pathway, in which the intermediates abundance is the highest in the total ion chromatograms. Pathway 1 can be considered as a minor or secondary pathway in CIP degradation process. The extent of mineralization of CIP was also investigated during the catalytic degradation process using the hexapod-like pyrite nanosheets mineral cluster catalyst (Fig. S5). The total organic carbon (TOC) concentration of the CIP solution decreased to 0 after 30 min reaction, suggesting that these intermediates would be fully mineralized by reactive species into low-molecular-mass byproducts, such as CO_2 and H_2O.

Based on the above results and analyzes, the removal mechanism of ciprofloxacin by the hexapod-like pyrite nanosheets mineral clusters was proposed and presented in Scheme 2. Ciprofloxacin could be rapidly adsorbed on the hexapod-like pyrite nanosheets mineral clusters surface *via* the electrostatic attraction, hydrophobic interaction, and van der Waals interactions. CIP could be directly oxidized and decomposed by $^{\bullet}OH_{ads}$ and $^{\bullet}OH_{bulk}$ through a series of heterogeneous and homogeneous Fenton reactions. These results prove that the hexapod-like pyrite nanosheets mineral clusters do not only provide the high surface area for adsorption of ciprofloxacin, but also act as a combination of surface catalysis at solid-liquid interface and homogeneously catalyzed process by leached/dissolved Fe^{2+}/Fe^{3+} to efficiently remove adsorbed ciprofloxacin as well as aqueous ciprofloxacin.

3.7. Toxicity predictions of CIP solution during the degradation process

To predict and understand the toxicity of CIP and its degradation generated products during pyrite Fenton catalytic degradation to aquatic organisms, the acute and chronic toxicities were calculated at three trophic levels with EPI Suite software with ECOSAR program. As Fig. 7 and Table S1 show, the acute toxicity was estimated as LC_{50} for fish and daphnia, and EC_{50} for green algae, and these data were 13,131.42, 1240.43, and 1621.63 mg/L for CIP, respectively. Chronic toxicity values (ChVs) of CIP were 1553.59, 81.27, and 455.22 mg/L for fish, daphnia, and green algae, respectively. This indicates that CIP is not harmful to aquatic organisms based on Chinese hazard evaluation guidelines for new chemical substances (HJ/T 154–2004) and European Union criteria [12,68].

For the chronic and acute toxicities of intermediates, most intermediates were non-harmful to three aquatic organisms except for P3, P5, P6, P9 and P13. The LC_{50}s for fish and ChVs for green algae of all the intermediates in three degradation pathways were higher than 10.0 and 1.0 mg/ L, respectively, suggesting that all these intermediates are not acutely toxic to fish but not chronically toxic to green algae. For

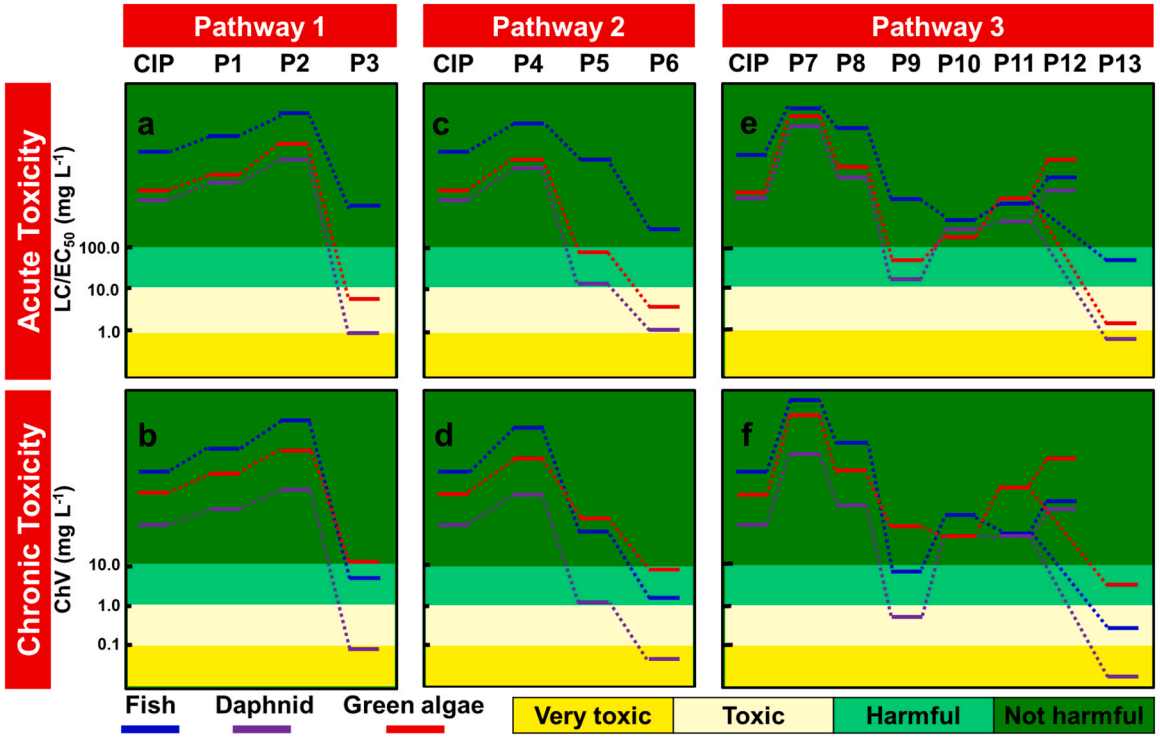

Fig. 7. Acute and chronic toxicity evolution of CIP and its degradation intermediates toward three aquatic organisms using EPI Suite software with ECOSAR program.

degradation pathways 1 and 2, chronic and acute toxicities at three trophic levels decreased initially and then increased. Whereas a complex trend of both toxicity evolutions of degradation intermediates was observed in pathways 3. P3 and P6 were very toxic to daphnia, toxic to green algae, and harmful to fish. P5 was harmful to green algae and daphnia. P9 was toxic to daphnia, and harmful to fish and green algae. Furthermore, P13 was very toxic to daphnia, and toxic to green algae and fish. Overall, the hazardous intermediates would be produced during the heterogeneous Fenton catalytic degradation of CIP using the hexapod-like pyrite nanosheets mineral cluster catalyst. However, these products could be further detoxified by reactive species through decomposing and transforming to CO_2 and H_2O with sufficient treated time, indicating this heterogeneous Fenton catalyst is very effective in detoxifying CIP [68].

4. Conclusions

In summary, a novel hexapod-like pyrite nanosheets mineral cluster catalyst was successfully prepared using a facile hydrothermal method. This catalyst could effectively remove CIP through adsorption and heterogeneous Fenton catalytic reaction, and it also possessed a higher catalytic activity and wider optimum pH than classical homogeneous Fenton process. The adsorption and degradation of CIP was highly pH dependent. $^{\bullet}OH$ was the main ROS responsible for the CIP degradation. The halide ions of Br^- and I^- exhibited a remarkable inhibition effect on pyrite heterogeneous Fenton degradation of CIP than Cl^- due to the formation of the less-reactive radicals $Br^{\bullet}$, $I^{\bullet}$, $Br_2^{\bullet-}$, or $I_2^{\bullet-}$, which could not react with CIP. The inhibition effect by higher concentration of F^- may be attributed to the coordination of fluoride to dissolved Fe(III) to form insoluble salts and less Fenton reactive complex. Several toxic intermediates produced during the catalytic degradation of ciprofloxacin, but they could be fully mineralized and detoxified with sufficient treated time. This study indicated that the hexapod-like pyrite nanosheets mineral cluster could be served as promising materials to apply in sustainable remediation of wastewater treatment especially for organic contaminated wastewater.

CRediT authorship contribution statement

Xin Nie: Methodology, Formal analysis, Writing – original draft, Investigation. **Guiying Li**: Validation. **Shanshan Li**: Data curation. **Yingmei Luo**: Formal analysis. **Wenming Luo**: Validation. **Quan Wan:** Supervision, Conceptualization. **Taicheng An:** Supervision, Conceptualization.

Declaration of Competing Interest

The authors declare that they have no known competing financial interests or personal relationships that could have appeared to influence the work reported in this paper.

Acknowledgements

This work was financially supported by the B-type Strategic Priority Program of the Chinese Academy of Sciences (XDB41000000), Guizhou Provincial Science and Technology Projects ([2020]1Z039), National Natural Science Foundation of China (41902041, 41872046), the Opening Fund of State Key Laboratory of Ore Deposit Geochemistry (201602). The thanks also given to Dr. Hai Yang and Dr. Jibin An for their help of data curation.

Appendix A. Supplementary material

Supplementary data associated with this article can be found in the online version at doi:10.1016/j.apcatb.2021.120734.

References

[1] A. Mirzaei, Z. Chen, F. Haghighat, L. Yerushalmi, Removal of pharmaceuticals from water by homo/heterogonous Fenton-type processes – a review, Chemosphere 174 (2017) 665–688.
[2] C. Boix, M. Ibanez, D. Fabregat-Safont, E. Morales, L. Pastor, J.V. Sancho, J. E. Sanchez-Ramirez, F. Hernandez, Behaviour of emerging contaminants in sewage sludge after anaerobic digestion, Chemosphere 163 (2016) 296–304.
[3] A.C. Singer, H. Shaw, V. Rhodes, A. Hart, Review of antimicrobial resistance in the environment and its relevance to environmental regulators, Front. Microbiol. 7 (2016) 22.
[4] G. Li, H. Yang, T. An, Y. Lu, Antibiotics elimination and risk reduction at two drinking water treatment plants by using different conventional treatment techniques, Ecotoxicol. Environ. Saf. 158 (2018) 154–161.
[5] Q. Zhang, G. Ying, C. Pan, Y. Liu, J. Zhao, Comprehensive evaluation of antibiotics emission and fate in the river basins of China: source analysis, multimedia modeling, and linkage to bacterial resistance, Environ. Sci. Technol. 49 (2015) 6772–6782.
[6] G.S. Zhang, W.Y. Li, S. Chen, W. Zhou, J.P. Chen, Problems of conventional disinfection and new sterilization methods for antibiotic resistance control, Chemosphere 254 (2020), 126831.
[7] X. Liu, J.C. Steele, X.Z. Meng, Usage, residue, and human health risk of antibiotics in Chinese aquaculture: a review, Environ. Pollut. 223 (2017) 161–169.
[8] M. Qiao, G.G. Ying, A.C. Singer, Y.G. Zhu, Review of antibiotic resistance in China and its environment, Environ. Int. 110 (2018) 160–172.
[9] H. Yin, X. Chen, G. Li, W. Wang, P.K. Wong, T. An, Can photocatalytic technology facilitate conjugative transfer of ARGs in bacteria at the interface of natural sphalerite under different light irradiation? Appl. Catal. B: Environ. 287 (2021), 119977.
[10] D.L. Cheng, H.H. Ngo, W.S. Guo, S.W. Chang, D.D. Nguyen, Y.W. Liu, X.B. Zhang, X. Shan, Y. Liu, Contribution of antibiotics to the fate of antibiotic resistance genes in anaerobic treatment processes of swine wastewater: a review, Bioresour. Technol. 299 (2020), 122654.
[11] O.M. Rodriguez-Narvaez, J.M. Peralta-Hernandez, A. Goonetilleke, E.R. Bandala, Treatment technologies for emerging contaminants in water: a review, Chem. Eng. J. 323 (2017) 361–380.
[12] G. Li, X. Nie, Y. Gao, T. An, Can environmental pharmaceuticals be photocatalytically degraded and completely mineralized in water using g-C_3N_4/TiO_2 under visible light irradiation?–implications of persistent toxic intermediates, Appl. Catal. B-Environ. 180 (2016) 726–732.
[13] W. Zhang, G. Li, H. Liu, J. Chen, S. Ma, M. Wen, J. Kong, T. An, Photocatalytic degradation mechanism of gaseous styrene over Au/TiO_2@CNTs: relevance of superficial state with deactivation mechanism, Appl. Catal. B: Environ. 272 (2020), 118969.
[14] H. Sun, G. Xie, D. He, L. Zhang, Ascorbic acid promoted magnetite Fenton degradation of alachlor: mechanistic insights and kinetic modeling, Appl. Catal. B: Environ. 267 (2020), 118383.
[15] M.E. Farshchi, H. Aghdasinia, A. Khataee, Heterogeneous Fenton reaction for elimination of Acid Yellow 36 in both fluidized-bed and stirred-tank reactors: computational fluid dynamics versus experiments, Water Res. 151 (2019) 203–214.
[16] D.B. Miklos, C. Remy, M. Jekel, K.G. Linden, J.E. Drewes, U. Hubner, Evaluation of advanced oxidation processes for water and wastewater treatment – a critical review, Water Res. 139 (2018) 118–131.
[17] E.M. Cuerda-Correa, M.F. Alexandre-Franco, C. Fernandez-Gonzalez, Advanced oxidation processes for the removal of antibiotics from water. An overview, Water 12 (2020) 102.
[18] J.J. Pignatello, E. Oliveros, A. MacKay, Advanced oxidation processes for organic contaminant destruction based on the Fenton reaction and related chemistry, Crit. Rev. Environ. Sci. Technol. 36 (2006) 1–84.
[19] Y.P. Zhu, R.L. Zhu, Y.F. Xi, J.X. Zhu, G.Q. Zhu, H.P. He, Strategies for enhancing the heterogeneous Fenton catalytic reactivity: a review, Appl. Catal. B: Environ. 255 (2019), 117739.
[20] S.O. Ganiyu, M.H. Zhou, C.A. Martinez-Huitle, Heterogeneous electro-Fenton and photoelectro-Fenton processes: a critical review of fundamental principles and application for water/wastewater treatment, Appl. Catal. B-Environ. 235 (2018) 103–129.
[21] D. Rickard, G.W. Luther, Chemistry of iron sulfides, Chem. Rev. 107 (2007) 514–562.
[22] D. Xia, Y. Li, G. Huang, C. Fong, T. An, G. Li, H. Yip, H. Zhao, A. Lu, P.K. Wong, Visible-light-driven inactivation of *Escherichia coli* K-12 over thermal treated natural pyrrhotite, Appl. Catal. B-Environ. 176 (2015) 749–756.
[23] B.B. Yu, X. Zhang, Y. Jiang, J. Liu, L. Gu, J.S. Hu, L.J. Wan, Solvent-induced oriented attachment growth of air-stable phasepure pyrite FeS_2 nanocrystals, J. Am. Chem. Soc. 137 (2015) 2211–2214.
[24] W. Liu, Y.Y. Wang, Z.H. Ai, L.Z. Zhang, Hydrothermal synthesis of FeS_2 as a high-efficiency fenton reagent to degrade alachlor via superoxide-mediated Fe(II)/Fe (III) cycle, ACS Appl. Mater. Interfaces 7 (2015) 28534–28544.
[25] X. Nie, S. Luo, M. Yang, P. Zeng, Z. Qin, W. Yu, Q. Wan, Facile hydrothermal synthesis of nanocubic pyrite crystals using greigite Fe_3S_4 and thiourea as precursors, Minerals 9 (2019) 273.
[26] H.Y. Xian, J.X. Zhu, X.L. Liang, H.P. He, Morphology controllable syntheses of micro- and nano-iron pyrite mono- and poly-crystals: a review, RSC Adv. 6 (2016) 31988–31999.

[27] T.T. Li, H.W. Liu, Z.N. Wu, Y. Liu, Z.X. Guo, H. Zhang, Seeded preparation of ultrathin FeS_2 nanosheets from Fe_3O_4 nanoparticles, Nanoscale 8 (2016) 11792–11796.
[28] C. Pan, M.T. Ou, Q.Z. Cheng, Y. Zhou, Y.K. Yu, Z.M. Li, F. Zhang, D.H. Xia, L. Mei, X.Y. Ji, Z-Scheme heterojunction functionalized pyrite nanosheets for modulating tumor microenvironment and strengthening photo/chemodynamic therapeutic effects, Adv. Funct. Mater. 30 (2020), 1906466.
[29] M. Caban-Acevedo, D. Liang, K.S. Chew, J.P. DeGrave, N.S. Kaiser, S. Jin, Synthesis, characterization, and variable range hopping transport of Pyrite (FeS_2) nanorods, nanobelts, and nanoplates, ACS Nano 7 (2013) 1731–1739.
[30] Y.X. Bai, J. Yeom, M. Yang, S.H. Cha, K. Sun, N.A. Kotov, Universal synthesis of single-phase pyrite FeS_2 nanoparticles, nanowires, and nanosheets, J. Phys. Chem. C 117 (2013) 2567–2573.
[31] T. Yang, Z.D. Gordon, C.K. Chan, Synthesis of hyperbranched perovskite nanostructures, Cryst. Growth Des. 13 (2013) 3901–3907.
[32] Y.L. Mikhlin, A.S. Romanchenko, I.P. Asanov, Oxidation of arsenopyrite and deposition of gold on the oxidized surfaces: a scanning probe microscopy, tunneling spectroscopy and XPS study, Geochim. Cosmochim. Acta 70 (2006) 4874–4888.
[33] M. Blanchard, M. Alfredsson, J. Brodholt, K. Wright, C.R.A. Catlow, Arsenic incorporation into FeS_2 pyrite and its influence on dissolution: a DFT study, Geochim. Cosmochim. Acta 71 (2007) 624–630.
[34] J.X. Zhu, H.Y. Xian, X.J. Lin, H.M. Tang, R.X. Du, Y.P. Yang, R.L. Zhu, X.L. Liang, J. M. Wei, H.H. Teng, H.P. He, Surface structure-dependent pyrite oxidation in relatively dry and moist air: implications for the reaction mechanism and sulfur evolution, Geochim. Cosmochim. Acta 228 (2018) 259–274.
[35] H.W. Nesbitt, G.M. Bancroft, A.R. Pratt, M.J. Scaini, Sulfur and iron surface states on fractured pyrite surfaces, Am. Mineral. 83 (1998) 1067–1076.
[36] J. Bebie, M.A.A. Schoonen, M. Fuhrmann, D.R. Strongin, Surface charge development on transition metal sulfides: an electrokinetic study, Geochim. Cosmochim. Acta 62 (1998) 633–642.
[37] F.L. Wang, Y.P. Feng, P. Chen, Y.F. Wang, Y.H. Su, Q.X. Zhang, Y.Q. Zeng, Z.J. Xie, H.J. Liu, Y. Liu, W.Y. Lv, G.G. Liu, Photocatalytic degradation of fluoroquinolone antibiotics using ordered mesoporous g-C_3N_4 under simulated sunlight irradiation: kinetics, mechanism, and antibacterial activity elimination, Appl. Catal. B-Environ. 227 (2018) 114–122.
[38] M. Kah, G. Sigmund, F. Xiao, T. Hofmann, Sorption of ionizable and ionic organic compounds to biochar, activated carbon and other carbonaceous materials, Water Res. 124 (2017) 673–692.
[39] A.S. Oberoi, Y.Y. Jia, H.Q. Zhang, S.K. Khanal, H. Lu, Insights into the fate and removal of antibiotics in engineered biological treatment systems: a critical review, Environ. Sci. Technol. 53 (2019) 7234–7264.
[40] H.B. Li, D. Zhang, X.Z. Han, B.S. Xing, Adsorption of antibiotic ciprofloxacin on carbon nanotubes: pH dependence and thermodynamics, Chemosphere 95 (2014) 150–155.
[41] X. Hu, X.J. Hu, Q.Q. Peng, L. Zhou, X.F. Tan, L.H. Jiang, C.F. Tang, H. Wang, S. H. Liu, Y.Q. Wang, Z.Q. Ning, Mechanisms underlying the photocatalytic degradation pathway of ciprofloxacin with heterogeneous TiO_2, Chem. Eng. J. 380 (2020), 122366.
[42] Q. Wu, X. Yang, J. Liu, X. Nie, Y. Huang, Y. Wen, J. Khan, W.U. Khan, M. Wu, T. An, Topotactic growth, selective adsorption, and adsorption-driven photocatalysis of protonated layered titanate nanosheets, ACS Appl. Mater. Interfaces 6 (2014) 17730–17739.
[43] C.H. Liu, Y.H. Chuang, H. Li, S.A. Boyd, B.J. Teppen, J.M. Gonzalez, C.T. Johnston, J. Lehmann, W. Zhang, Long-term sorption of lincomycin to biochars: the intertwined roles of pore diffusion and dissolved organic carbon, Water Res. 161 (2019) 108–118.
[44] H. Tekin, O. Bilkay, S.S. Ataberk, T.H. Balta, I.H. Ceribasi, F.D. Sanin, F.B. Dilek, U. Yetis, Use of Fenton oxidation to improve the biodegradability of a pharmaceutical wastewater, J. Hazard. Mater. 136 (2006) 258–265.
[45] X.X. Zhu, J.F. Li, B. Xie, D.Q. Feng, Y.M. Li, Accelerating effects of biochar for pyrite-catalyzed Fenton-like oxidation of herbicide 2,4-D, Chem. Eng. J. 391 (2020), 123605.
[46] I. Michael, E. Hapeshi, C. Michael, D. Fatta-Kassinos, Solar Fenton and solar TiO_2 catalytic treatment of ofloxacin in secondary treated effluents: evaluation of operational and kinetic parameters, Water Res. 44 (2010) 5450–5462.
[47] C. Kantar, O. Oral, O. Urken, N.A. Oz, S. Keskin, Oxidative degradation of chlorophenolic compounds with pyrite-Fenton process, Environ. Pollut. 247 (2019) 349–361.
[48] C. Kantar, Role of low molecular weight organic acids on pyrite dissolution in aqueous systems: implications for catalytic chromium (VI) treatment, Water Sci. Technol. 74 (2016) 99–109.
[49] C. Gil-Lozano, A.F. Davila, E. Losa-Adams, A.G. Fairen, L. Gago-Duport, Quantifying Fenton reaction pathways driven by self-generated H_2O_2 on pyrite surfaces, Sci. Rep. 7 (2017) 43703.
[50] Y.Q. Zhang, H.P. Tran, I. Hussain, Y.Q. Zhong, S.B. Huang, Degradation of p-chloroaniline by pyrite in aqueous solutions, Chem. Eng. J. 279 (2015) 396–401.
[51] Z.H. Diao, X.R. Xu, D. Jiang, G. Li, J.J. Liu, L.J. Kong, L.Z. Zuo, Enhanced catalytic degradation of ciprofloxacin with FeS_2/SiO_2 microspheres as heterogeneous Fenton catalyst: kinetics, reaction pathways and mechanism, J. Hazard. Mater. 327 (2017) 108–115.
[52] F.X. Deng, H. Olvera-Vargas, O. Garcia-Rodriguez, S. Qiu, J.X. Yang, O. Lefebvre, The synergistic effect of nickel-iron-foam and tripolyphosphate for enhancing the electro-Fenton process at circum-neutral pH, Chemosphere 201 (2018) 687–696.
[53] T. An, H. Yang, G. Li, W. Song, W.J. Cooper, X. Nie, Kinetics and mechanism of advanced oxidation processes (AOPs) in degradation of ciprofloxacin in water, Appl. Catal. B-Environ. 94 (2010) 288–294.
[54] T. An, H. Yang, W. Song, G. Li, H. Luo, W.J. Cooper, Mechanistic considerations for the advanced oxidation treatment of fluoroquinolone pharmaceutical compounds using TiO_2 heterogeneous catalysis, J. Phys. Chem. A 114 (2010) 2569–2575.
[55] H. Yang, G. Li, T. An, Y. Gao, J. Fu, Photocatalytic degradation kinetics and mechanism of environmental pharmaceuticals in aqueous suspension of TiO_2: a case of sulfa drugs, Catal. Today 153 (2010) 200–207.
[56] Y.J. Li, X.L. Qiao, Y.N. Zhang, C.Z. Zhou, H.J. Xie, J.W. Chen, Effects of halide ions on photodegradation of sulfonamide antibiotics: formation of halogenated intermediates, Water Res. 102 (2016) 405–412.
[57] R.E. Connick, L.G. Hepler, Z.Z. Hugus, J.W. Kury, W.M. Latimer, M.S. Tsao, The complexing of iron(Iii) by fluoride ions in aqueous solution – free energies, heats and entropies, J. Am. Chem. Soc. 78 (1956) 1827–1829.
[58] Y. Lei, S.S. Cheng, N. Luo, X. Yang, T.C. An, Rate constants and mechanisms of the reactions of $Cl^{\bullet}$ and $Cl_2^{\bullet-}$ with trace organic contaminants, Environ. Sci. Technol. 53 (2019) 11170–11182.
[59] S. Gligorovski, R. Strekowski, S. Barbati, D. Vione, Addition and correction to environmental implications of hydroxyl radicals (•OH), Chem. Rev. 118 (2018) 2296, 2296-2296.
[60] T. Suzuki, K. Yamada, M. Inukai, Effects of chloride, bromide, and iodide upon decomposition of nucleosides induced by ultrasound in neutral solution, Nucleosides Nucleotides Nucleic Acids 29 (2010) 606–615.
[61] A. Machulek, J.E.F. Moraes, C. Vautier-Giongo, C.A. Silverio, L.C. Friedrich, C.A. O. Nascimento, M.C. Gonzalez, F.H. Quina, Abatement of the inhibitory effect of chloride anions on the photo-Fenton process, Environ. Sci. Technol. 41 (2007) 8459–8463.
[62] F. Yang, B. Sheng, Z.H. Wang, R.X. Yuan, Y. Xue, X.X. Wang, Q.Z. Liu, J.S. Liu, An often-overestimated adverse effect of halides in heat/persulfate-based degradation of wastewater contaminants, Environ. Int. 130 (2019), 104918.
[63] X. Nie, G. Li, M. Gao, H. Sun, X. Liu, H. Zhao, P. Wong, T. An, Comparative study on the photoelectrocatalytic inactivation of *Escherichia coli* K-12 and its mutant *Escherichia coli* BW25113 using TiO_2 nanotubes as a photoanode, Appl. Catal. B-Environ. 147 (2014) 562–570.
[64] H.H. Cai, X. Liu, J. Zou, J.Y. Xiao, B.L. Yuan, F. Li, Q.F. Cheng, Multi-wavelength spectrophotometric determination of hydrogen peroxide in water with peroxidase-catalyzed oxidation of ABTS, Chemosphere 193 (2018) 833–839.
[65] X.Y. Yang, H. Wei, K.B. Li, Q. He, J.C. Xie, J.T. Zhang, Iodine-enhanced ultrasound degradation of sulfamethazine in water, Ultrason. Sonochem. 42 (2018) 759–767.
[66] Y.F. Ji, C. Ferronato, A. Salvador, X. Yang, J.M. Chovelon, Degradation of ciprofloxacin and sulfamethoxazole by ferrous-activated persulfate: implications for remediation of groundwater contaminated by antibiotics, Sci. Total Environ. 472 (2014) 800–808.
[67] A.Q. Wang, H. Wang, H. Deng, S. Wang, W. Shi, Z.X. Yi, R.L. Qiu, K. Yan, Controllable synthesis of mesoporous manganese oxide microsphere efficient for photo-Fenton-like removal of fluoroquinolone antibiotics, Appl. Catal. B-Environ. 248 (2019) 298–308.
[68] Y. Gao, T. An, H. Fang, Y. Ji, G. Li, Computational consideration on advanced oxidation degradation of phenolic preservative, methylparaben, in water: mechanisms, kinetics, and toxicity assessments, J. Hazard. Mater. 278 (2014) 417–425.